Correspondence to:
F. Hoffmann,
fa.hoffmann@lmu.de

Between Broadening and Narrowing: How Mixing Affects the Width of the Droplet Size Distribution

Jung-Sub Lim[1] ![ORCID] **and Fabian Hoffmann[1]** ![ORCID]

[1]Meteorological Institute, Ludwig Maximilian University of Munich, Munich, Germany

Abstract Entrainment and mixing play an essential role in shaping the droplet size distribution (DSD), with commensurate effects on cloud radiative properties or precipitation formation. In this paper, we use a model that considers all relevant scales related to entrainment and mixing by employing the linear eddy model (LEM) as a subgrid-scale (SGS) mixing model, coupled with a large-eddy simulation model and a Lagrangian cloud model (LCM) for a single cumulus congestus cloud. We confirm that the DSD is broadened toward small-size droplets during homogeneous mixing. During inhomogeneous mixing, the DSD width remains almost unchanged. The DSD width can also be narrowed after mixing. We show that this happens when DSD is broadened toward small-size droplets, which evaporate rapidly, while larger droplets are almost unaffected. In addition, when droplets ascend during mixing, DSD narrowing is caused when the adiabatic increase in supersaturation is slower than the average droplet evaporation, allowing only the largest droplets to benefit from the newly produced supersaturation. The narrowing mixing scenario prevents clouds from having too broad DSDs and causes the DSD relative dispersion to converge around 0.2 to 0.4. As this scenario is more frequent when the LEM SGS model is used, our results indicate that adequately modeling turbulent mixing is necessary to represent a realistic DSD shape.

Plain Language Summary Clouds are always in contact with the surrounding air. Because the air outside the cloud is drier than the cloud, cloud droplets tend to evaporate when it enters the cloud. The size of the cloud droplets after evaporation can vary depending on the timescales of turbulent mixing and droplet evaporation. If the dry air mixes quickly, all droplets evaporate simultaneously. If the dry air is mixed slowly, only the droplets exposed to the dry air evaporate. However, this mixing occurs on small scales that traditional cloud models cannot account for. To account for this, we use a special model capable of representing all relevant scales. We confirm previous theoretical work that when mixing is fast, all droplets evaporate and the mean droplet size decreases. When mixing is slow, some droplets evaporate completely, but the average droplet size remains constant. We also observe cases where only small droplets evaporate while large droplets barely change. This scenario happens when there are many small droplets to evaporate or when additional moisture from cloud motion prevents larger droplets from evaporating completely.

1. Introduction

Cumulus clouds play an important role in the Earth's climate system by affecting precipitation, the radiation budget, and energy transport (Boucher et al., 2013). Clouds are influenced by complex multi-scale turbulent motions ranging from the kilometer to the millimeter scale, between which entrainment and mixing dominates the cloud dynamics. Due to this complexity, the representation of cumulus clouds remains a major source of uncertainty in numerical weather prediction and global climate models.

Entrainment and mixing have been extensively investigated over the past decades (e.g., Baker et al., 1980; Blyth, 1993; Hoffmann et al., 2019; Krueger et al., 1997; Lehmann et al., 2009). Entrainment and mixing were regarded as crucial mechanisms for broadening the droplet size distribution (DSD), particularly in the radius range between 15 and 40 μm, the so-called size gap, in which neither condensational nor collisional growth is effective. How droplets grow within this gap is still a critical question in warm rain initiation (Devenish et al., 2012; Grabowski & Wang, 2013).

Most fundamentally, entrainment describes the transport of dry and warm ambient air into clouds, where these air masses mix turbulently and eventually homogenize. During this process, droplets exposed to recently entrained air evaporate and contribute to the saturation of the dry air. The resultant mixing scenarios have been categorized based on the timescales describing the turbulent mixing and the microphysical response by evaporation (e.g., Baker & Latham, 1979; Lehmann et al., 2009; Lu et al., 2018).

If one assumes that the turbulent mixing is so fast that the entrained air is mixed immediately with the cloudy air, all droplets in the mixture will experience the same subsaturation and evaporate partially. In this case of (extreme) homogeneous mixing, the cloud droplet mean volume radius,

$$r_v = \left(\frac{3\text{LWC}}{4\pi \rho_l N} \right)^{\frac{1}{3}},$$

$$(1)$$

where ρ_l is the liquid water density, decreases proportionally to the change in liquid water content (LWC), while the cloud droplet concentration (N) remains unchanged. On the other hand, when turbulent mixing is relatively slow, droplets surrounded by the entrained air begin to evaporate before the air masses are homogenized. This scenario is called (extreme) inhomogeneous mixing, during which droplets in the subsaturated region of the cloud completely evaporate until the entrained air is saturated while droplets in the cloud remain unchanged. Thus, in this case, only N decreases, while r_v remains unchanged. Note that intermediate mixing scenarios are expected to affect both N and r_v.

In recent years, it has been suggested that other effects, for example, the faster evaporation of small droplets and dynamical motions of the cloud (Luo et al., 2020, 2021, 2022; Pinsky et al., 2016; Tölle & Krueger, 2014), or the so-called secondary activation of entrained aerosol particles above cloud base (Chandrakar et al., 2021; Krueger et al., 2008; Lu et al., 2020; Luo et al., 2022) can also affect how mixing changes the DSD in ways that are not covered by the aforementioned idealized framework of homogeneous and inhomogeneous mixing. In particular, it was suggested that DSDs could be either broadened or narrowed during mixing inside an updraft when secondary activation is possible or not (Krueger et al., 2008; Lu et al., 2020).

Classifying different mixing scenarios and investigating their effects on the DSD is important as large-scale cloud properties such as the cloud albedo can substantially differ depending on the mixing scenario (e.g., Chosson et al., 2007; Grabowski, 2006; Slawinska et al., 2008). Nonetheless, even with relatively high-resolution modeling approaches such as large-eddy simulation (LES), turbulent mixing is usually assumed to be homogeneous on unresolved scales, the so-called sub-grid scale (SGS). However, the assumption of pure homogeneous mixing only applies to lengthscales below a few decimeters. At larger scales, even strong turbulence cannot mix environmental and cloudy air fast enough and the mixing tends to be inhomogeneous (Lehmann et al., 2009). As the typical resolution of LES is tens of meters, the impact of homogeneous mixing is overestimated without using an appropriate SGS model to account for small-scale turbulence and mixing processes explicitly (Krueger, 1993).

Thus, the effects of different mixing scenarios need to be investigated in more sophisticated modeling frameworks considering SGS processes. So far, this has been done in idealized frameworks with many prescribed or simplified parameters (e.g., relative humidity of entrained airmasses, turbulent kinetic dissipation rate) (Desai et al., 2021; Kumar et al., 2013; Lu et al., 2013; Luo et al., 2022; Tölle & Krueger, 2014). However, questions still remain whether these findings are applicable to more realistic settings where the large-scale cloud dynamics determine these parameters naturally.

It has recently been found useful to combine SGS models with Lagrangian cloud models (LCMs) as a scale-crossing approach to investigate mixing in clouds (Chandrakar et al., 2021; Hoffmann et al., 2019; Hoffmann & Feingold, 2019). The LCM is a cloud microphysical model that represents cloud droplets, but also aerosol particles and raindrops, as Lagrangian particles, so-called superdroplets (Andrejczuk et al., 2006; Grabowski et al., 2019; Hoffmann et al., 2015; Oh & Noh, 2022; Shima et al., 2009, 2020). Specifically, a novel modeling approach known as the *L3 model* was developed by Hoffmann et al. (2019) as an extension of the LCM to investigate inhomogeneous mixing effects on stratocumulus clouds (Hoffmann & Feingold, 2019). In the L3 model, the linear eddy model (LEM) developed by Kerstein (1988) and further applied to cloud microphysics studies starting from Krueger (1993) and Su et al. (1998) is used as an SGS model to represent the turbulent mixing process down to the Kolmogorov scale. By properly representing SGS supersaturation fluctuations, mixing varies naturally between homogeneous and inhomogeneous in L3 without prescribing the mixing scenario. Using this ability, this study will investigate how and where different mixing scenarios occur in a single cumulus congestus cloud and how these mixing scenarios affect the DSD.

This paper is organized as follows. Section 2 presents the L3 model framework and simulation settings, while Section 3 introduces the applied method for classifying different mixing scenarios. General results are shown in Section 4, and the causes of the DSD narrowing mixing scenario are thoroughly discussed in Section 5. In Section 6, we conclude our paper.

2. Model and Simulation Setting

2.1. The L3 Model

In this study, we investigate entrainment and mixing events in a single cumulus congestus cloud using an LES model coupled with an LCM and LEM. The approach to combine these three models is called L3 (LES-LCM-LEM), which was developed by Hoffmann et al. (2019). The dynamical core of our simulation is the System for Atmospheric Modeling (SAM) by Khairoutdinov and Randall (2003), a nonhydrostatic, anelastic LES model.

The LCM simulates particle-based cloud microphysics process using computational particles (i.e., LCM particles), each representing a number of identical hydrometeors of the same properties (e.g., liquid radius, location, aerosol mass). In the L3 model, the absolute supersaturation fluctuation (δ'_n) of a virtual air volume around each LCM particle is stored as a new LCM particle property and updated throughout the particle growth history. By doing so, each LCM particle memorizes δ'_n from the previous time step. Here, the subscript n indicates the nth LCM particle.

The LEM is an explicit turbulence and mixing model developed by Kerstein (1988). In the L3 model, the LEM is used for redistributing δ'_n among the LCM particles in the same LES grid box, depending on the SGS turbulence degree. LCM particles in the same LES grid box are aligned into a one-dimensional array. The LEM grid size is determined by dividing the LES vertical grid size by the number of LCM particles. Segments are randomly chosen from this one-dimensional array and internally rearranged to mimic turbulent compression and folding using the so-called triplet map (Kerstein, 1988). In this paper, the LEM resolution is approximately 40 cm. This is substantially higher than that of the LES (50 m) but still larger than the physical Kolmogorov lengthscale. Thus, molecular diffusion in the LEM is replaced by an appropriately scaled turbulent diffusion coefficient to consider the effect of turbulence on the scales the LEM cannot resolve (Krueger et al., 1997). Interested readers can refer to Hoffmann et al. (2019), Hoffmann and Feingold (2019), and Hoffmann (2020) for details on applying the LEM in the L3 model.

In the L3 model, the actual supersaturation that determines the condensational growth can vary for each LCM particle in the same LES grid box depending on δ'_n, and the LES-resolved absolute supersaturation, $\bar{\delta} = \bar{q}_v - q_s(\bar{T}, p)$, where $\bar{q}_v$ is the LES water vapor mixing ratio and $q_s(\bar{T}, p)$ is the saturation vapor mixing ratio calculated from the LES absolute temperature $\bar{T}$ and hydrostatic pressure p. Thus, droplet growth is determined as

$$\frac{dr_n}{dt} = \frac{G}{(r_n + r_0)}\left(\frac{\bar{\delta} + \delta'_n}{q_s(\bar{T}, p)} - \frac{a}{r_n} + \frac{br_{N,n}^3}{r_n^3}\right)f_v(r_n), \tag{2}$$

where r_n is the radius of the droplet represented by the nth LCM particle, $r_0 \approx 1.86$ µm is a lengthscale to consider gas kinetic effects (Kogan, 1991; Mordy, 1959), $r_{N,n}$ is the dry aerosol radius of the nth droplet, a and b are terms associated with curvature effect and solute effect, respectively, f_v is a parameterized ventilation effect depending on the droplet radius, and the growth parameter $G = (F_d + F_k)^{-1}$ summarizes the effects of vapor diffusion and heat conduction on condensation, with F_d, a coefficient associated with vapor diffusion, and F_k, associated with heat conduction [see Yau and Rogers (1996), pp. 87–88, 102, 116) for details on Equation (2)].

2.2. Simulation Settings

This study investigates a single cumulus congestus cloud based on the Small Cumulus Microphysics Study (SCMS) field experiment following the simulation case developed by Lasher-Trapp et al. (2005). The total model domain size is $10 \times 10 \times 8$ km in the x, y, and z directions, respectively, with isotropic 50 m grid spacing. The simulation is carried out for 3 h with a timestep $\Delta t = 0.5$ s. Initial random perturbations of the potential temperature and specific humidity are prescribed in the lowest 1 km of the model domain to initiate turbulent convection. For the first hour, horizontally homogeneous surface sensible heat (0.1 K m s^{-1}) and latent heat fluxes (4.0×10^{-5} kg kg^{-1} m s^{-1}) are prescribed. For the last 2 h, Gaussian distributed surface fluxes of sensible heat and latent heat are prescribed in the center of the horizontal domain that force the cloud to develop. The respective maxima are 0.3 K m s^{-1} and 4.0×10^{-5} kg kg^{-1} m s^{-1}, with a half-width of the Gaussian distribution of 1.7 km. The surface momentum flux is calculated from a constant friction velocity (0.28 m s^{-1}) and the LES surface horizontal wind velocity. For a detailed description of the initialization of the cumulus congestus cloud, readers can refer to Chandrakar et al. (2021).

In each grid box, 120 LCM particles are initialized, where each LCM particle represents the same number of droplets. The initial spatial position of each LCM particle in each LES grid box is chosen randomly. In the initial stage, all LCM particles are initialized as sea-salt aerosol particles, which dry radius $r_{N,n}$ follows a log-normal distribution that has two modes with geometric mean radii of $r_{m,1} = 0.03$ μm and $r_{m,2} = 0.14$ μm and geometric standard deviations of $\sigma_{r,1} = 1.28$ and $\sigma_{r,2} = 1.75$. Initial aerosol number concentrations for the two modes are $N_1 = 990.0$ cm^{-3} and $N_2 = 165.0$ cm^{-3}. The initial aerosol radii in each LES grid box are randomly distributed, and the corresponding initial liquid radii are determined by equilibrating them to the initial LES saturation ratio. Additional simulations have been conducted without the LEM under the same conditions. In this study, collision-coalescence and sedimentation of droplets are not considered, as particles barely exceed 10 μm in radius and thus do not collide.

3. Classifying Different Mixing Scenarios: The Homogeneous Mixing Degree

As previously mentioned, classifying mixing scenarios is an important goal of this paper. One way to predict the mixing scenario is to compare the microphysical response timescale (τ_{micro}) to the turbulent mixing timescale (τ_{mix}) using the Damköhler number,

$$\text{Da} = \frac{\tau_{mix}}{\tau_{micro}}. \tag{3}$$

Here, τ_{mix} is defined as

$$\tau_{mix} = \left(l^2 / \varepsilon \right)^{1/3}, \tag{4}$$

where l is the lengthscale of a scalar inhomogeneity, such as a blob of entrained air that breaks down to the Kolmogorov lengthscale through turbulent motions at a given turbulence kinetic energy dissipation rate ε (Baker et al., 1980; Baker & Latham, 1979). When Da $\ll 1$, turbulent mixing is much faster than the microphysical response, and homogeneous mixing is favored. When Da $\gg 1$, droplets respond to the subsaturation of the entrained air before the airmasses are completely mixed. In this case, inhomogeneous mixing is favored.

Various types of timescales can represent τ_{micro}. One example is the phase relaxation timescale,

$$\tau_{phase} = (4\pi D_v N r_m)^{-1}. \tag{5}$$

τ_{phase} represents the time to reach saturation by the evaporation of droplets, where r_m is the mean droplet radius and D_v the molecular diffusion coefficient for water vapor (Kumar et al., 2013; Lehmann et al., 2009; Squires, 1952; Tölle & Krueger, 2014). Another example is the evaporation timescale,

$$\tau_{evap} = \frac{r_v^2}{G(1 - \text{RH}_{entrained})}, \tag{6}$$

which estimates the time for a droplet to evaporate during entrainment, where $\text{RH}_{entrained}$ is the relative humidity of the entrained air (Jarecka et al., 2013; Kumar et al., 2013; Lehmann et al., 2009; Tölle & Krueger, 2014). Note that we use r_v in Equation 6 instead of an individual droplet radius to obtain a DSD-wide τ_{evap}. Other microphysical response times and choosing the optimal microphysical timescale were discussed in several studies (e.g., Lu et al., 2018; Tölle & Krueger, 2014).

Although Da can indicate which mixing scenario occurs, it does not contain information about the actual changes in the DSD. Thus, microphysical mixing diagrams are often used to determine changes in N and LWC, or equivalently r_v^3, depending on a specified mixing scenario (Burnet & Brenguier, 2007; Gerber et al., 2008). This allows us to predict the microphysical values related to the DSD change at the end of a mixing process.

Based on the mixing diagram, early attempts have been made to parameterize the effects of different mixing scenarios using

$$N_f = N_i \left(\frac{\text{LWC}_f}{\text{LWC}_i} \right)^{\alpha}, \tag{7}$$

where the subscripts i and f indicate the time or state before and after mixing, respectively, and α varies from 0 to 1 depending on the assumed mixing scenario (Andrejczuk et al., 2006; Morrison & Grabowski, 2008). In

the extreme homogeneous mixing scenario, N remains unchanged, so α is 0; and in the extreme inhomogeneous mixing scenario, N decreases proportional to LWC, so α is 1. However, α has to be predetermined to use this parameterization. Therefore, this parameterization requires information on how α varies spatially and temporally.

If a simulation can track N and LWC changes during mixing, α can be estimated from a simple transformation of Equation 7, that is

$$\alpha = \frac{\ln(N_f/N_i)}{\ln(LWC_f/LWC_i)}. \tag{8}$$

Thus, α can be used as a metric to estimate the mixing scenario based on the changes in N and LWC.

Note that other attempts were made to diagnose the mixing scenario by comparing the observed N and LWC with adiabatic values of N and LWC at the same level (Lu et al., 2013; S. Gao et al., 2020). However, recent studies suggest that using α alone may limit the parameterization of DSD shape changes. Thus, studies suggest including other parameters, such as the DSD shape before mixing, the relative humidity (RH), or the number of droplets entrained along the environmental air for a more comprehensive parameterization (Luo et al., 2020; Xu et al., 2022; Z. Gao et al., 2018). Note further that our α is in reverse relationship to the "homogeneous mixing degree" used in the aforementioned studies. Thus, we call α the "inhomogeneous mixing degree" (IHMD).

In this study, the IHMD is calculated only in the grid boxes where mixing occurs, where we define mixing as a decrease in LWC over a time t_{lag} inside the cloud. To apply Equation 7, LWC and N are required to be larger than 0 after t_{lag}. Grid boxes with LWC > 0.01 g kg^{-1} are considered cloudy, where droplets larger than 1 μm are considered cloud droplets that contribute to LWC and N. Further, the IHMD is only analyzed in grid boxes with RH < 95% before mixing. This constraint is necessary to distinguish different mixing scenarios, for which substantial evaporation is necessary (A. Korolev et al., 2016).

To do this, we analyze all LCM particles inside the same LES grid box after mixing. The LCM particles store various parameters that have been obtained before mixing, that is, t_{lag} ago, allowing us to obtain N_i, LWC$_i$, but also RH and other quantities before mixing. Note that the RH is determined using $\left(\overline{\delta} + \delta'_n\right)/q_s + 1$, that is, the RH determining the diffusional growth of the LCM particles. The aforementioned quantities are calculated as the average (or the respective sum) of the LCM particles located in the same LES grid box after mixing, using values obtained before mixing, that is, from a potentially different LES grid box. Finally, we estimate N_f and LWC$_f$ with droplets already activated before mixing, not considering secondary activation in the IHMD estimation. However, the relatively small effect of secondary activation on the DSD during mixing will be discussed in Section 5.

As the actual times when mixing starts and ends are indeterminable in real clouds and three-dimensional simulations, we have to prescribe the timescale t_{lag} over which mixing is assessed. To account for the initial dilution and evaporation during mixing events, t_{lag} should be longer than typical droplet reaction timescales (e.g., $\tau_{phase} \approx 10$ s) to allow for droplet evaporation and associated changes in N. It was found that microphysical variables are highly variant during the initial 10 s of the mixing process but soon reach a steady state after it (Kumar et al., 2017; Lu et al., 2014; Luo et al., 2020). Furthermore, if t_{lag} is too long, many droplets can move substantially, along with substantial adiabatic cooling and warming. Therefore, we compare N and LWC changes for $t_{lag} = 30$ s when estimating the IHMD. We confirm that our conclusions hold for t_{lag} between 20 and 30 s, and the t_{lag} dependency on the results is discussed in Section 5.3.

4. Results

4.1. Characteristics of the Mixing Scenarios

We will begin our assessment with a general overview of the cloud development. Figures 1 and 2 show the vertical and horizontal cross sections of the LWC and IHMD (Figures 1a–1e and 2a–2e) and adiabatic fraction (AF) (Figures 1f–1j and 2f–2j) at 7,260–8,460 s. The LWC cross sections are overlaid with the IHMD. The AF is a frequently used quantity in entrainment and mixing studies to explain the degree of dilution in clouds. In this study, we estimate AF using the LCM particles as a tracer, similar to the approach described in Eytan et al. (2021), where they used a passive scalar tracer to estimate the AF. Thus, every LCM particle below the cloud base height (around 1 km) is marked; and the AF is estimated by the ratio between the number of marked LCM particles to
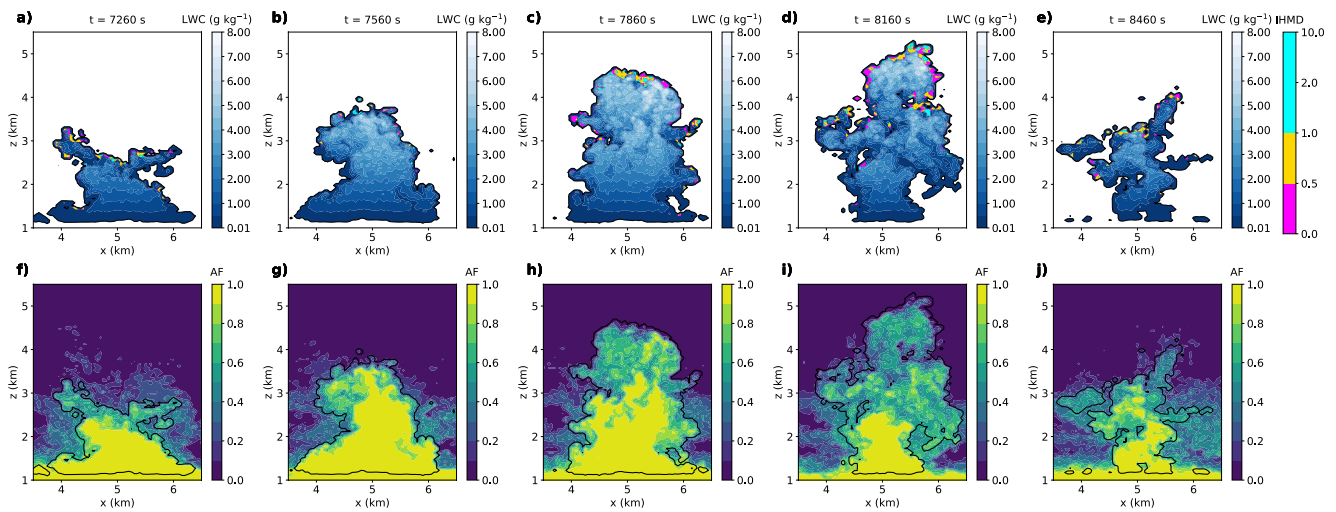
Figure 1. Vertical cross sections of LWC (a–e) and AF (f–j) at simulation times between 7,260 and 8,460 s at $y = 5$ km. Cross sections of IHMD are laid over the LWC cross sections with three different colors (magenta: $0 \leq$ IHMD ≤ 0.5, yellow: $0.5 <$ IHMD ≤ 1.0 and cyan: IHMD > 1).

the total number of LCM particles in the same grid box. If the cloudy grid box is purely adiabatic, AF = 1, and AF decreases when external unmarked LCM particles from above the cloud base are entrained. Therefore, in this study, unless otherwise stated, the results were obtained with data collected from grid boxes where entrainment and mixing occurs, that is, diluted (AF < 1), evaporated ($\text{LWC}_{\text{after}}/\text{LWC}_{\text{before}} < 1$) and with IHMD ≥ 0.

Initially, the undiluted adiabatic air rises over the lifted condensation level, where condensation forms the cloud base (Figures 1a and 2a). As the dilution starts from the cloud edges during the developing stage (7,560–7,860 s), the cloud starts to lose its buoyant force (Figures 1b and 1c and 2b and 2c). Finally, the cloud starts to dissipate from the most diluted cloud edges and becomes universally diluted (8,160–8,460 s) (Figures 1i, 1j, and 2i–2j). It is apparent that entrainment and mixing shape the fractious cloudy volumes away from the undiluted cloud core in the dissipating stage of the cloud life cycle (Figures 1d, 1e, and 2d–2e). As the entrainment and mixing characteristics are versatile in space and time, the results are analyzed between 7,560 and 8,160 s to cover the most actively developing and decaying cloud stages.

In observational studies, the mixing scattering diagram is often used to evaluate the prevalent mixing scenario, using the relation between LWC and r_v to their respective maximum (or adiabatic) value (e.g., Burnet & Brenguier, 2007; Gerber et al., 2008; Lehmann et al., 2009; Yum et al., 2015). Unlike observational data, we can
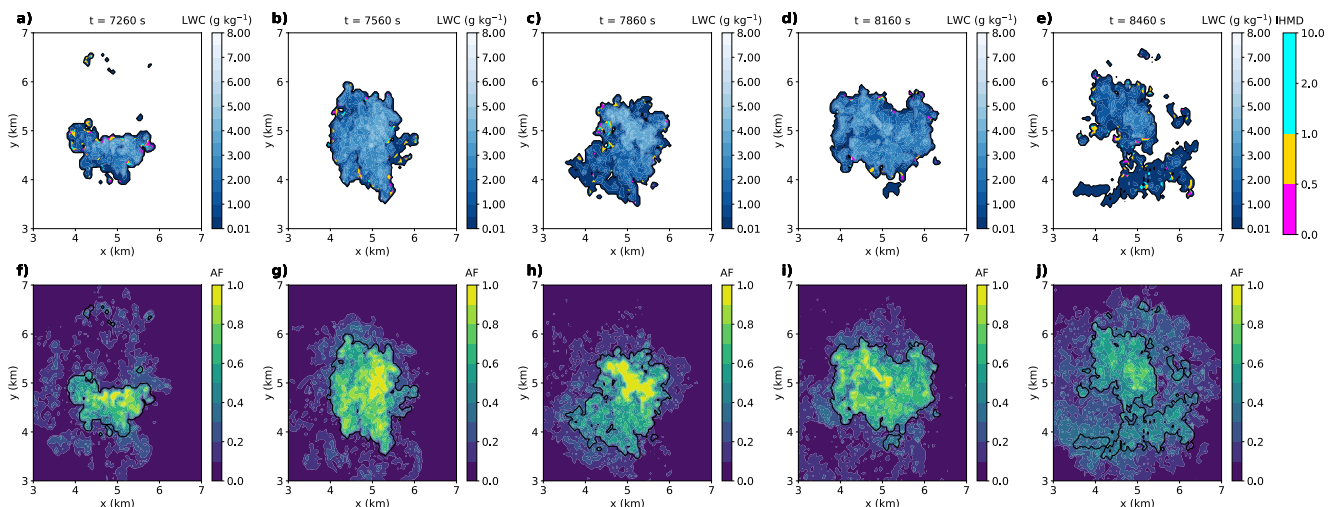

Figure 2. Same as in Figure 1 but for horizontal cross sections at the model vertical level of $z = 3$ km.
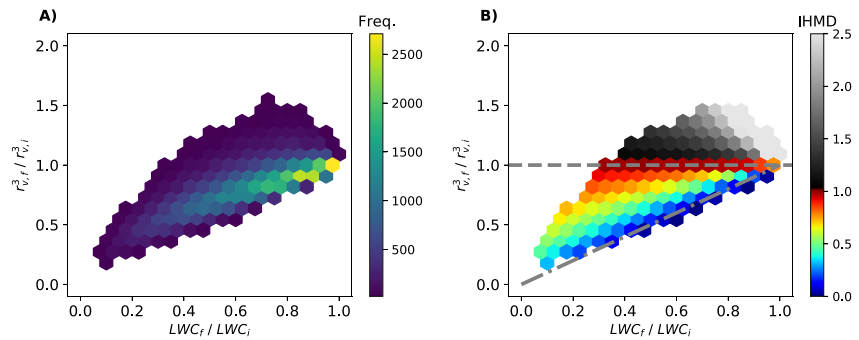
Figure 3. Binned mixing scattering diagrams for data collected between 7,560 and 8,160 s from volumes that experience entrainment and mixing. The colors of each bin indicate (a) the frequency of points in that bin and (b) the bin-averaged IHMD. The abscissa depicts the ratio between the LWC before (LWC_i) and after (LWC_f) mixing, and the ordinate depicts the ratio between r_v^3 before $\left(r_{v,i}^3\right)$ and after $\left(r_{v,f}^3\right)$ mixing. The gray dash-dotted line indicates the extreme homogeneous mixing limit, and the gray dashed line indicates the extreme inhomogeneous mixing limit.

track the r_v and LWC changes during mixing. Thus, we estimate the IHMD with the actual LWC and r_v changes during t_{lag}. Figure 3a shows the frequency distribution of mixing events in the mixing scattering diagram and Figure 3b shows the corresponding mean IHMD value.

Figure 3 shows that the IHMD can depict the expected changes in r_v^3 and LWC under each mixing scenario. Most of the points were found to be distributed between the extreme homogeneous mixing boundary (dash-dotted line, where $r_{v,f}^3/r_{v,i}^3 = LWC_f/LWC_i$, and thus $N_i = N_f$) and the extreme inhomogeneous mixing boundary (dashed line, where $r_{v,f}/r_{v,i} = 1$). Near the extreme homogeneous mixing boundary, the IHMD is 0, and near the extreme inhomogeneous mixing boundary, IHMD is 1, as expected. We should note that the point where extreme homogeneous and extreme inhomogeneous mixing overlap is omitted from the discussion. In this so-called degenerate mixing scenario (A. Korolev et al., 2016), mixing scenarios cannot be determined because of the minimal LWC change.

Most interestingly, we find special cases where r_v^3 increases while LWC decreases, shown in the regions where the IHMD is over 1 (Figure 3b, gray-scaled bins). An increase in r_v^3 is not expected in the classical mixing concept, but recently this phenomenon gained interest from studies using idealized parcel model simulations (Krueger et al., 2008; Luo et al., 2021; Pinsky et al., 2016; Tölle & Krueger, 2014). We will discuss this mixing scenario case further in the following sections.

To understand mixing in the mixing scattering diagram better, Figure 4 shows further parameters that potentially affect the mixing process. Here, all microphysical properties are estimated from the values experienced by all LCM particles before mixing (i.e., their radius and supersaturation before t_{lag}). First, the two microphysical response timescales τ_{evp} and τ_{phase} show different relationships to the IHMD (Figures 4a and 4b compared to Figure 3b). It is found that τ_{evp} is longer along the extreme homogeneous boundary (dash-dotted line), while it is shorter near the extreme inhomogeneous boundary (dashed line). This confirms that mixing tends to be more homogeneous when the microphysical response is slow. Surprisingly, τ_{phase} is not substantially related to the IHMD. In clouds, the relative humidity of the entrained air can vary, and the speed of evaporation is closely related to the degree of subsaturation, see (6), which is not considered in τ_{phase}. Therefore, τ_{evp} might be more generally applied for mixing scenario classification, as suggested in Lu et al. (2018).

ε is also expected to be related to the mixing scenarios via τ_{mix}. However, IHMD and ε are not uniquely related to each other (Figure 4c compared to Figure 3b), which is in good agreement with Luo et al. (2022). This might be due to the fact that ε can vary substantially during the mixing processes, making a single value, as used in Figure 4c, inadequate for representing the entire process. In addition, eddy lengthscale l, also affecting τ_{mix}, might also be important to relate ε to the mixing scenario but is usually unknown. Therefore, determining τ_{mix} is more complicated than finding a microphysical response time.

Another important factor in the mixing process is the RH of the entrained air, $RH_{entrained}$, and cloudy air, RH_{cloud}, both determined before mixing. We estimate $RH_{entrained}$ by averaging the supersaturation of the entrained LCM particles, and RH_{cloud} by averaging the supersaturation of LCM particles originating from the cloud base in each grid box before t_{lag}. Overall, RH_{cloud} is higher than $RH_{entrained}$ as expected, but both values show a wide range of
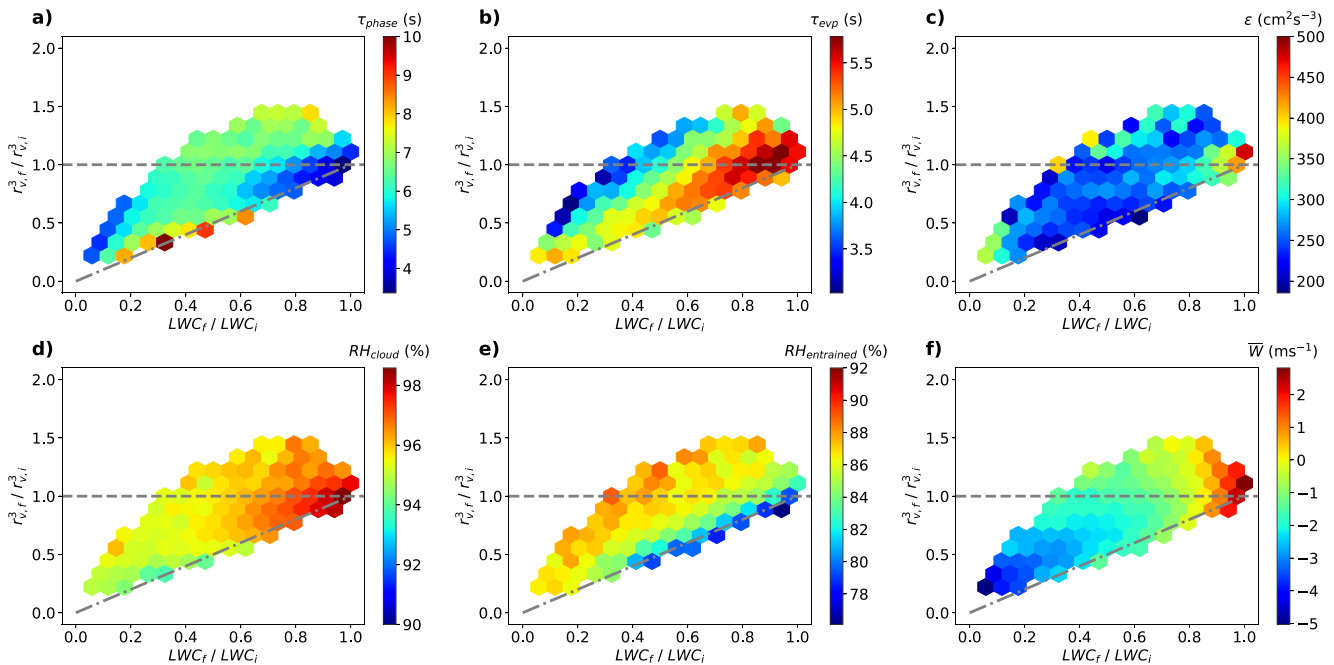
Figure 4. Binned mixing scattering diagram for bin-averaged (a) phase relaxation timescale before mixing, (b) evaporation timescale before mixing, (c) dissipation rate before mixing, (d) RH_{cloud} before mixing, (e) $RH_{entrained}$ before mixing and (f) mean updraft velocity of droplets during t_{lag}. Only bins containing more than 25 data points are shown.

variability. RH_{cloud} can be lowered if previous entrainment events have already diluted the cloud. The variability in $RH_{entrained}$ is caused by the entrainment of previously detrained cloudy air, which happens more often as the cloud ages (Lehmann et al., 2009). It is found that RH_{cloud} is mostly related to the LWC dilution while $RH_{entrained}$ is more related to the mixing scenarios (Figures 4d and 4e). When RH_{cloud} is low, LWC will decrease more, because all droplets experience a more subsaturated environment. When $RH_{entrained}$ is low, more droplets need to evaporate to restore saturation. Thus, all droplets will be affected, leading to more homogeneous mixing (dashed-dotted line). When $RH_{entrained}$ is high, however, mixing tends to be more inhomogeneous because saturation can be reached faster, and thus before all droplets evaporate completely (Figure 4e). Interestingly, $r_{v,f}^3 / r_{v,i}^3$ tends to increase when both RH_{cloud} and $RH_{entrained}$ are high.

Furthermore, the vertical velocity shows a distinct distribution in the mixing scattering diagram (Figure 4f). The mean LCM particle vertical velocity $\left(\overline{W} \right)$ is calculated as

$$\overline{W} = \frac{z_f - z_i}{t_{lag}},\tag{9}$$

where z_f and z_i indicate the height of an LCM particle after and before mixing, respectively. Adiabatic warming in the downdraft region causes the RH to decrease and accelerates the evaporation of droplets. Thus, LWC_f/LWC_i is smaller within a strong downdraft. In the cases between inhomogeneous and homogeneous mixing boundaries (between the dashed and dash-dotted lines), droplets experience a mild downdraft, which is typical for the cloud edge (e.g., Heus & Jonker, 2008). Droplets can also ascend during mixing, which is mainly happening at the cloud top during the actively growing stages of the cloud (cf. Figure 1b), which is mostly associated with IHMD >1 (cf. Figure 3b).

4.2. DSD Change in Each Mixing Scenario

Figure 5 shows different DSDs before and after mixing. We show DSD changes for (intermediate) homogeneous mixing scenarios ($0 \leq IHMD \leq 0.5$), (intermediate) inhomogeneous mixing scenarios ($0.5 < IHMD \leq 1.0$), and mixing scenarios in which IHMD > 1. DSDs after mixing are calculated with droplets in the same LES grid box, and DSDs before mixing are calculated with the same droplets based on their previous properties, that is, their radius before t_{lag}. We should note that these regions are already diluted before mixing as entrainment and mixing
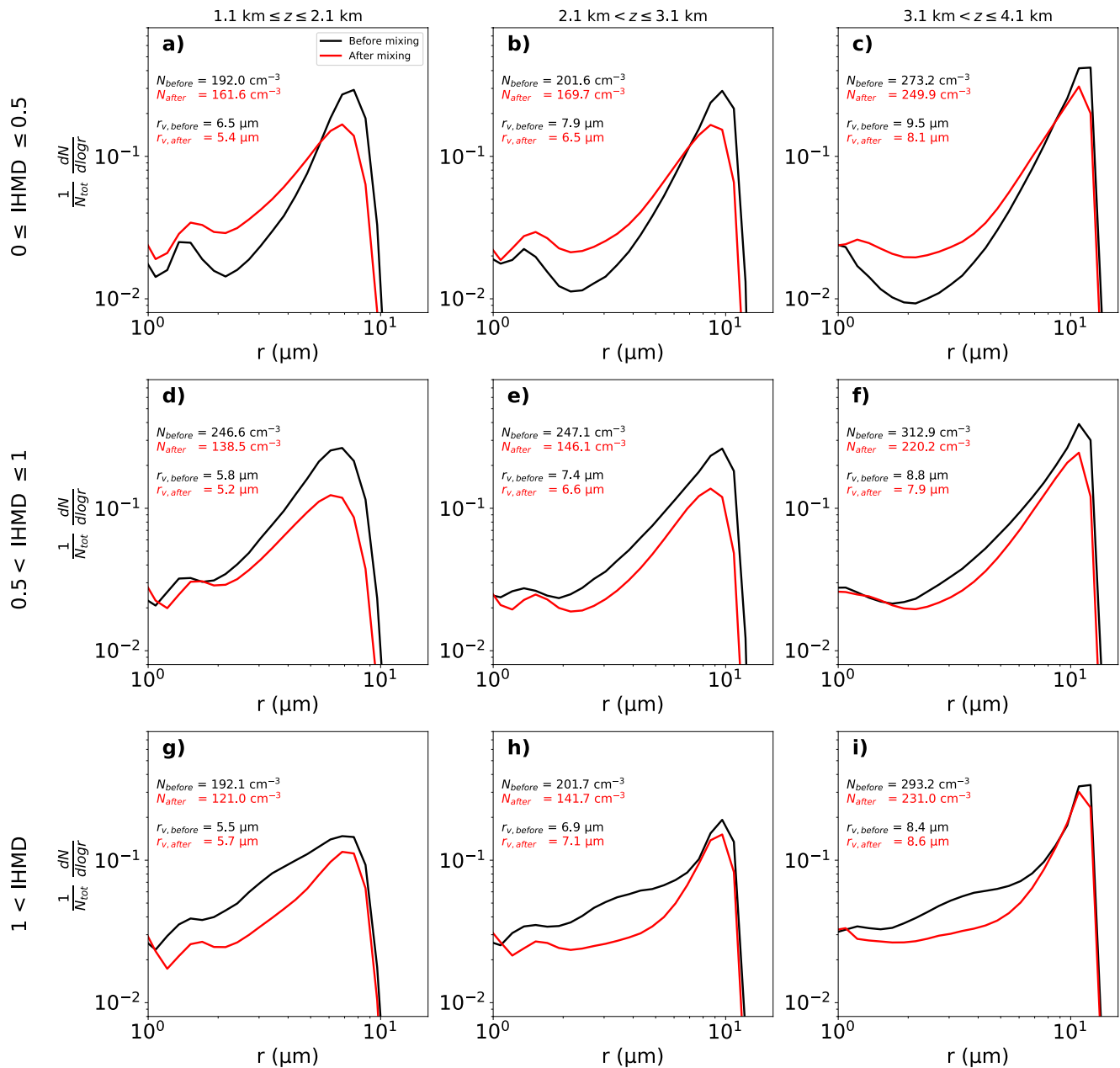
Figure 5. Normalized DSDs before (black) and after (red) mixing for homogeneous cases (a, b, and c, $0 \leq \text{IHMD} \leq 0.5$), for inhomogeneous cases (d, e, and f, $0.5 < \text{IHMD} \leq 1.0$) and mixing cases with $\text{IHMD} > 1$ (g, h, and i). N_{tot} is the number concentration of all aerosol particles and cloud droplets in a certain volume and used for normalization. Data is collected between 7,560 and 8,160 s at different heights ((a), (d), (g) 1.1–2.1 km; (b), (e), (h) 2.1–3.1 km; and (c), (f), (i) 3.1–4.1 km), where entrainment and mixing occurs ($\text{IHMD} \geq 0$). Cloud droplet number concentration and the mean volume radius before (N_{before} and $r_{v,before}$) and after (N_{after} and $r_{v,after}$) mixing are also indicated.

mainly occur at the cloud edges regardless of the mixing scenario (Figures 1 and 2), causing broader DSDs throughout the analyzed cloud.

When the mixing is classified as homogeneous ($0 \leq \text{IHMD} \leq 0.5$), the DSDs broaden to smaller sizes as all droplets evaporate partially (Figures 5a–5c). In this case, the DSDs change asymmetrically, resulting in an increase in the number of small droplets (say $r < 6\,\mu m$) and a decrease in the number of large droplets, in agreement with our classical understanding of homogeneous mixing. As we also consider intermediate mixing scenarios, N can decrease after mixing. However, the decrease in N after mixing is the smallest, and the decrease in r_v is largest in the homogeneous mixing scenarios compared to the other scenarios, see N and r_v indicated in Figure 5.

When the mixing is classified as inhomogeneous ($0.5 <$ IHMD ≤ 1.0), N decreases substantially and the DSDs shrink symmetrically at all droplet sizes, while the width of the DSD remains almost unchanged (Figures 5d–5f). This is also in agreement with our classical understanding of inhomogeneous mixing. The most noticeable difference is that the small droplet number concentration decreases after mixing, whereas it increases after mixing in the homogeneous case. Thus, the mean droplet radius does not change substantially as the DSDs are neither shifted nor broadened in the inhomogeneous case, see $r_{\mathrm{v,before}}$ and $r_{\mathrm{v,after}}$ indicated in Figures 5d–5f.

Finally, the most interesting result is that the DSD is narrowed when IHMD > 1 (Figures 5g–5i). In this scenario, many small droplets completely evaporate while the large droplets remain almost unchanged. This narrows the DSD toward the large droplet peak. Thus, this is a special case where the mean droplet radius increases, see $r_{\mathrm{v,before}}$ and $r_{\mathrm{v,after}}$ indicated in Figures 5g–5i. In particular, r_{v}^{3} can increase as N decreases without substantially decreasing the LWC, as the evaporation of small droplets negligibly affects the LWC. The necessary abundance of small droplets for this narrowing scenario can be quantified with $r_{\mathrm{m}} - \sigma_{\mathrm{r}}$, where σ_{r} is the droplet radius standard deviation (Tölle & Krueger, 2014). We find that the $r_{\mathrm{m}} - \sigma_{\mathrm{r}}$ is smaller in the DSD narrowing cases (~ 3.8 µm) than in the homogeneous cases (~ 5.4 µm) and the inhomogeneous cases (~ 4.4 µm). Besides, r_{m} is also smaller in the DSD narrowing scenario than in the homogeneous scenarios and inhomogeneous scenarios, implying more small droplets.

In the narrowing scenario, the DSD shape changes differently from the other two. We will call this mixing scenario *"narrowing mixing scenario,"* and discuss if this separate definition can be justified in Section 5.2.1. All in all, we find that the three mixing scenarios change the width of the DSD in three different ways, broadening (homogeneous), unchanging (inhomogeneous), and narrowing (*narrowing mixing scenario*).

5. The Narrowing Mixing Scenario

5.1. When Does the Narrowing Mixing Scenario Occur?

We found that various microphysical properties affect the mixing scenarios. The *narrowing mixing scenario* is favored when $\mathrm{RH}_{\mathrm{entrained}}$ before mixing is high, and when droplets ascend during mixing $\left(\overline{W} > 0 \right)$ (Figures 4c, 4d, and 4f). In addition, we found that each mixing scenario affects the DSD width differently (Figure 5). Therefore, we investigate DSD shape changes using r_{m}, σ_{r} and the relative dispersion, $d_{\mathrm{r}} = \sigma_{\mathrm{r}}/r_{\mathrm{m}}$, and their relative change during mixing, $\rho_{x} = x_{\mathrm{after}}/x_{\mathrm{before}}$, where $x = d_{\mathrm{r}}$, σ_{r}, and r_{m} (Figure 6).

When d_{r} and σ_{r} are large ($d_{\mathrm{r,before}} > 0.4$ and $\sigma_{\mathrm{r,before}} > 3$ µm), the IHMD tends to be larger than 1, and the DSD is more likely to narrow after mixing ($\rho_{d_{\mathrm{r}}} < 1$ and $\rho_{\sigma_{\mathrm{r}}} < 1$ in Figures 6b and 6d). Moreover, r_{m} increases during the *narrowing mixing scenario* largely independent of $r_{\mathrm{m,before}}$, while smaller r_{m} are more favored (Figure 6f). In contrast to σ_{r} alone, a large d_{r} indicates how close r_{m} is to zero (i.e., $1 - d_{\mathrm{r}} = (r_{\mathrm{m}} - \sigma_{\mathrm{r}})/r_{\mathrm{m}}$), implying the DSD is broadened to small droplets. Thus, we confirm that the *narrowing mixing scenario* is favored when DSD is not just broad but also broadened toward small-size droplets.

On the other hand, when d_{r} is small and the DSD is narrow ($d_{\mathrm{r,before}} < 0.2$ and $\sigma_{\mathrm{r}} < 2$ µm), mixing will result in DSD broadening. We find that homogeneous mixing is favored when $r_{\mathrm{m,before}}$ is large, and d_{r} is small, implying all droplets are similarly large (Figures 6b and 6f). This indicates slow droplet evaporation, making complete evaporation of droplets less likely.

Inhomogeneous mixing is favored when $r_{\mathrm{m,before}}$ is small (Figure 6f), implying that some droplets may completely evaporate during mixing. When d_{r} is around 0.2 to 0.4, the d_{r} will most likely remain constant (Figure 6b). Due to these three distinct ways of DSD width change, we find that a d_{r} between 0.2 and 0.4 is favored in the cloud (95% confidence ellipse in Figure 6a). This suggests that the different mixing scenarios may balance each other as the increased number of small droplets due to the homogeneous mixing (or other processes such as the secondary activation) can trigger the *narrowing mixing scenario* to reduce the number of small droplets.

5.2. Why Does the Narrowing Mixing Scenario Occur?

We find that the *narrowing mixing scenario* is favored when (1) the DSD is broad with many small droplets, and (2) droplets ascend during mixing. Furthermore, we confirmed that the DSD narrowing is mainly due to the complete evaporation of small droplets while large droplets remain unchanged (Figures 5g–5i). This begs the question: How can only the large droplets survive?
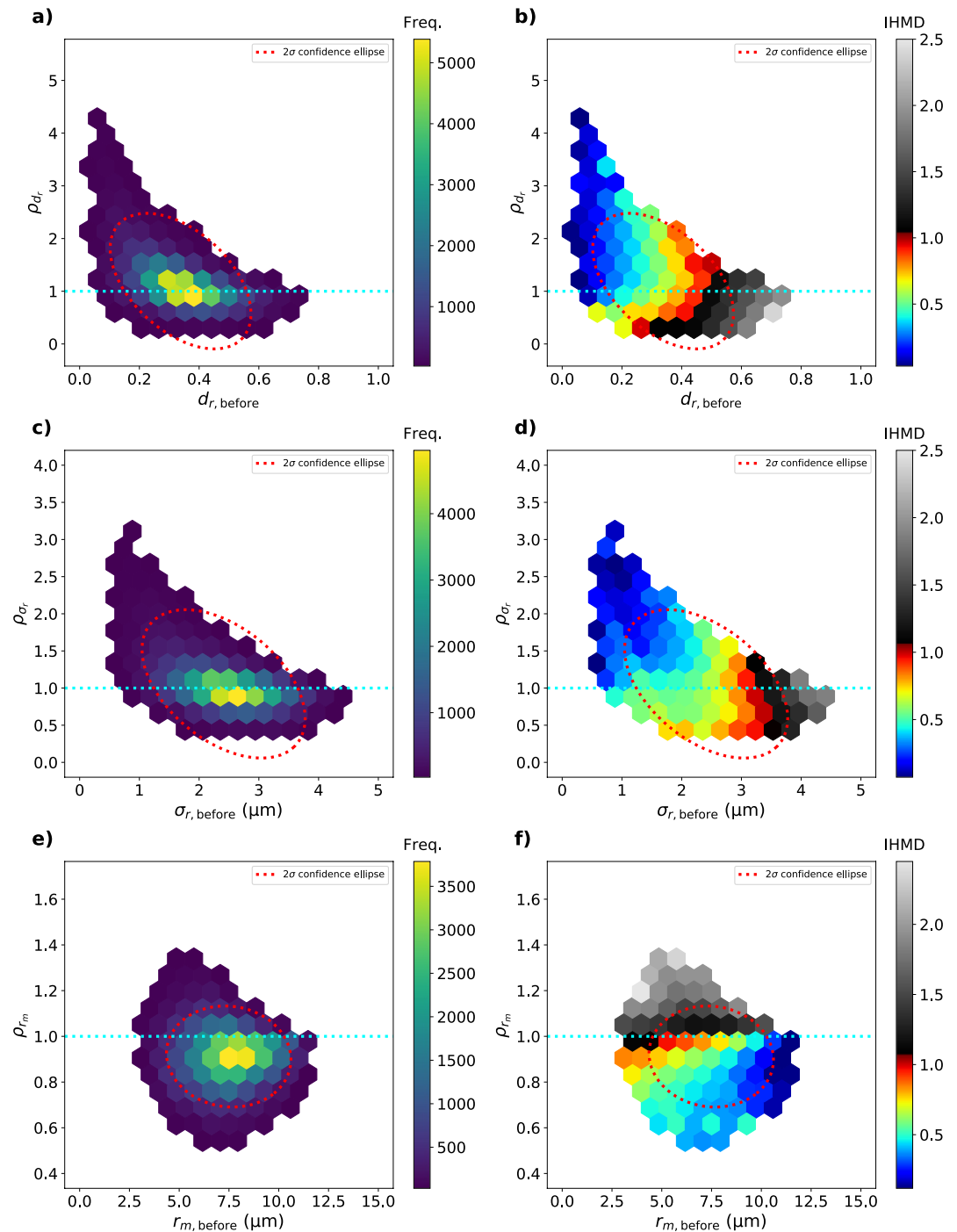
Figure 6. Binned plot with frequency in each bin (panels a, c, and e) and bin-averaged IHMD (panels b, d, and f). The abscissa represents the droplet radius relative dispersion (d_r) before mixing (panels a and b), the droplet radius standard deviation (σ_r) before mixing (panels c and d), and the mean droplet radius (r_m) before mixing (panels e and f), and the ordinate shows their respective relative change during mixing, ρ_x, where x is d_r, σ_r, and r_m. The dotted cyan line indicates where $\rho_x = 1$, and the dotted red line indicates a 95% confidence ellipse, where statistics inside the ellipse are reliable. Only bins containing more than 25 data points are shown.

5.2.1. Different Evaporation Speed of Differently Sized Droplets

The first explanation relates to the different evaporation speeds due to different droplet sizes. Based on the equation for droplet diffusional growth (2), the condensation or evaporation rate is inversely proportional to the

droplet radius, $|\mathrm{d}r/\mathrm{d}t| \propto r^{-1}$. This means that when droplets of various sizes coexist in a subsaturated environment, smaller droplets change their radius faster than larger droplets. Thus, when $d_{r,\text{before}}$ is large, and small droplets are abundant, complete evaporation of small droplets, which evaporate faster than larger droplets, can be sufficient to reach saturation, and the *narrowing mixing scenario* takes place. Therefore, high $\mathrm{RH}_{\text{entrained}}$ and $\mathrm{RH}_{\text{cloud}}$, make the *narrowing mixing scenario* more likely (Luo et al., 2022; Tölle & Krueger, 2014).

If homogeneous mixing takes place, every cloud droplet should be exposed to the same subsaturation. Nonetheless, small droplets will evaporate faster and restore saturation before large droplets evaporate substantially, which narrows the DSD (Pinsky et al., 2016). Similarly, during inhomogeneous mixing, only small droplets evaporate completely in the initially subsaturated air while large droplets survive (Hoffmann et al., 2019), which will also result in DSD narrowing. Thus, the *narrowing mixing scenario* does not depend on whether the mixing occurs homogeneously or inhomogeneously. It depends on the large variability in droplet sizes and hence evaporation speeds, favoring the complete evaporation of the smallest droplets over the larger ones, causing the observed narrowing of the spectrum.

5.2.2. Supersaturation Replenishment by the Updraft

Adiabatic cooling during ascent increases the supersaturation, while droplet condensation decreases the supersaturation by absorbing water vapor. Therefore, changes in supersaturation in an ascending volume of air can be approximated as

$$\frac{\mathrm{d}S}{\mathrm{d}t} = a_0 w - \frac{S}{\tau_{\text{phase}}}, \tag{10}$$

where a_0 is a thermodynamic variable that varies with temperature (A. V. Korolev & Mazin, 2003). If one assumes entrainment and mixing as an isobaric process, w is commonly neglected, and droplet evaporation will be the primary factor that restores the supersaturation during entrainment and mixing. However, we find that some droplets experience substantial ascending motions during entrainment and mixing (Figure 4f). Then, adiabatic cooling during ascent can also replenish supersaturation.

We can determine a characteristic timescale for the updraft velocity to restore saturation as

$$\tau_{\text{up}} = \left| \frac{S}{a_0 w} \right|. \tag{11}$$

For $w = 10 \text{ m s}^{-1}$, $\tau_{\text{up}} = 18.6$ s for a temperature of 273 K and $S = -0.1$. Therefore, an updraft restores S slower than droplet evaporation (τ_{phase} and $\tau_{\text{evp}} < 10$ s in Figures 4a and 4b). Although the actual time for saturating a volume of air or the complete droplet evaporation can be slower than estimated by τ_{evp} or τ_{phase} (e.g., Lehmann et al., 2009), small droplets may evaporate completely in a shorter time. For RH = 80%, τ_{evp} for 1 μm droplets is 0.05 s, while it is 20 s for a 20 μm droplet. Therefore, the adiabatic cooling by the updraft will predominantly benefit large droplets, which tend to evaporate more slowly and thus survive. In other words, the different effects of updraft supersaturation replenishment on small and large droplets will intensify the *narrowing mixing scenario*.

The relationship between the IHMD, $d_{r,\text{before}}$, and $\overline{W}$ is shown in Figure 7. It is important to note that the *narrowing mixing scenario* occurs both in the downdraft and updraft regions. However, for the same $d_{r,\text{before}}$ (e.g., $d_{r,\text{before}} \sim 0.3$), mixing becomes more inhomogeneous as $\overline{W}$ increases, with the narrowing mixing scenario occurring at even larger $\overline{W}$. In particular, the *narrowing mixing scenario* can occur even for smaller $d_{r,\text{before}}$ if $\overline{W}$ is sufficiently strong (Figure 7b). Conversely, adiabatic warming in a downdraft, $\overline{W} < 0$, helps droplets to evaporate further and makes mixing more homogeneous. Thus, the *narrowing mixing scenario* is rare in substantial downdrafts $\left(\overline{W} < -5 \text{ m s}^{-1} \right)$.

As aerosol particles are inherently entrained during the entrainment and mixing process in our model, we find evidence of secondary activation in the updraft regions as in Krueger et al. (2008) and Chandrakar et al. (2021). However, comparable or even stronger deactivation of droplets is observed in the same region where the *narrowing mixing scenario* occurs, which, due to the evaporation of the smallest droplets, balances the addition of small droplets by secondary activation (Figures 7c and 7d). On the other hand, positive net activation rates generally broaden the DSD. In the homogeneous mixing scenario, the net activation rate can be positive due to the negligible amount of droplets deactivated, and activated droplets can contribute to DSD broadening toward smaller
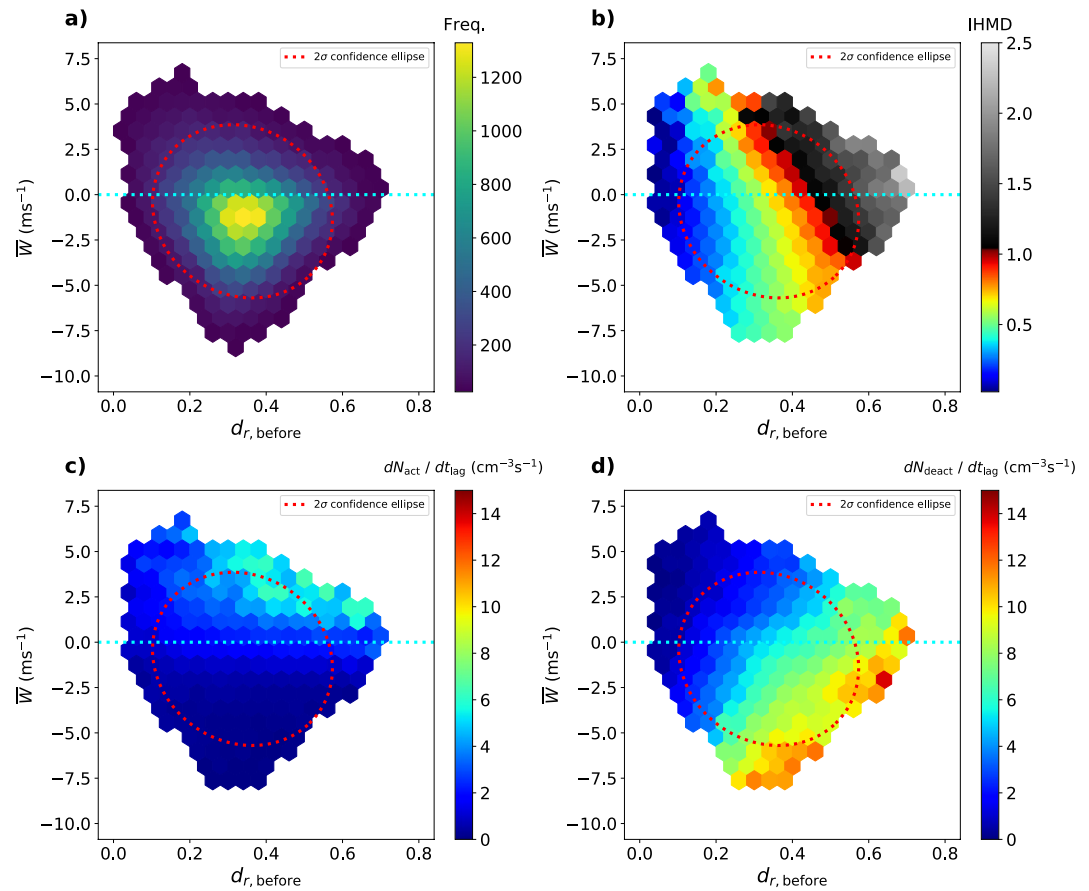
Figure 7. Binned plot with (a) frequency in each bin, (b) bin-averaged IHMD, (c) activation rate, and (d) deactivation rate during t_{lag} in a $d_{r,before}$ (abscissa) and the $\overline{W}$ (ordinate) phase space. The dotted cyan line indicates where $\overline{W} = 0$, and the dotted red line indicates a 95% confidence ellipse where statistics inside the ellipse are reliable. Only bins containing more than 25 data points are shown.

sizes. This is in good agreement with Krueger et al. (2008) and Luo et al. (2022), who found that DSDs can be broadened after mixing when ascending motions enable activation of entrained aerosol particles. However, the number of activated droplets is negligible in our simulation, even if the net activation rate is positive. Therefore, $d_{r,before}$ and supersaturation replenishment by droplet ascent are more related to the DSD shape change.

5.3. The Role of the Narrowing Mixing Scenario in Cumulus Cloud DSDs

Finally, it is intriguing to consider how the DSD shape in the cloud might change under the fairly rare *narrowing mixing scenario*. Figure 8a shows density distributions of IHMD for the cases with and without the LEM, essentially allowing or preventing explicit SGS mixing. We find that the IHMD distribution is slightly shifted to larger values with the LEM, meaning mixing tends to be more inhomogeneous, and the *narrowing mixing scenario* is more frequent than in the case without the LEM (Figure 8a).

Additionally, results from the simulation with LEM, with $t_{lag} = 20$ s for IHMD estimation, are shown (Figure 8a). We find that the IHMD distributions from $t_{lag} = 20$ and 30 s are nearly identical. However, due to the weaker LWC dilution during a shorter t_{lag}, extreme homogeneous mixing (IHMD ≈ 0) occurs more frequently with $t_{lag} = 20$ s. In general, t_{lag} between 20 and 30 s do not change our conclusions.

In Figures 8b–8d, the d_r, r_m, and σ_r frequency distribution for simulations with and without the LEM are shown. To minimize the divergent development of the flow fields once different SGS mixing schemes are used, the simulation without LEM starts from the flow field of the simulation with LEM at 7,440 s, that is, $2 \times t_{lag}$ before analysis. Only the results between 7,560 s and 8,160 s are analyzed. Without the LEM, d_r and σ_r are larger, while
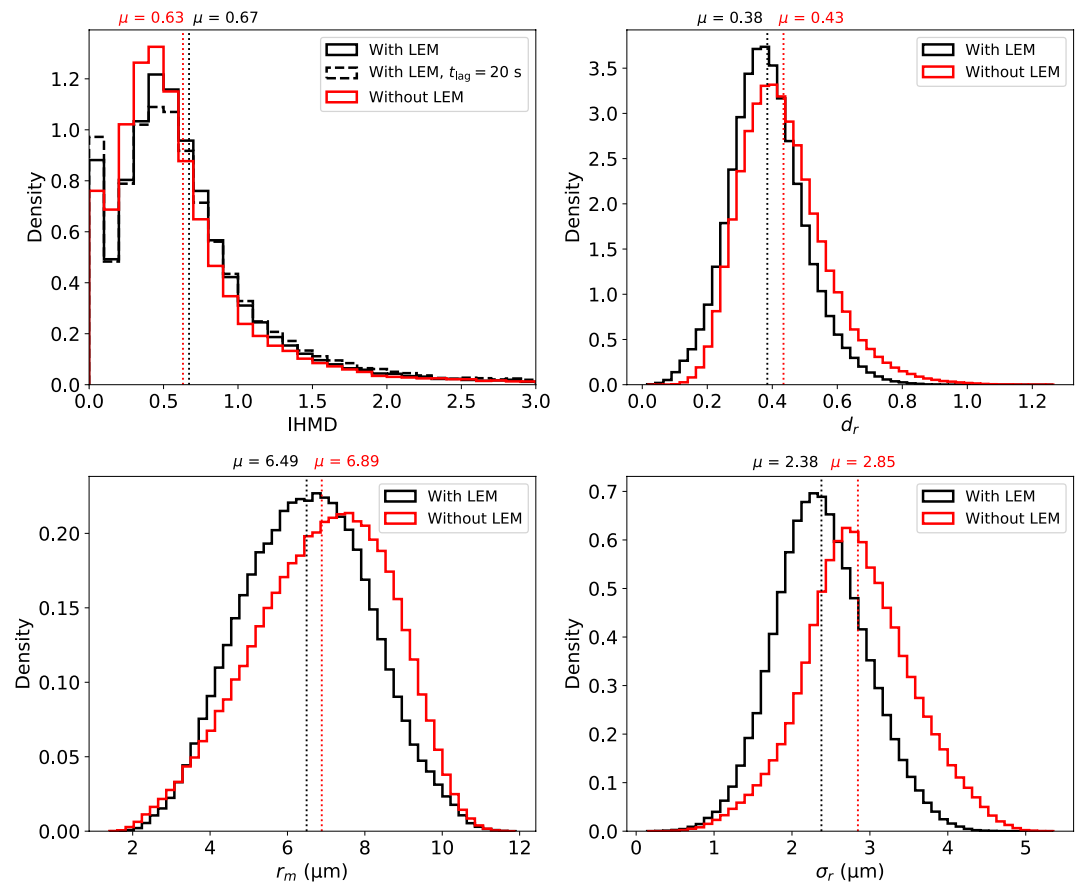
Figure 8. Density distribution of (a) IHMD, (b) d_r, (c) r_m and (d) σ_r in the regions where entrainment and mixing occurs for simulations with (black) and without (red) the LEM. The mean (μ) of each distribution is also indicated.

the r_m distributions are similar but also more negatively skewed. This implies a broader DSD width without the LEM where mixing events are inherently more homogeneous, with a lower chance of the *narrowing mixing scenario* (Figure 8a). The less frequent occurrence of a mechanism that narrows wide DSDs results in overall larger d_r and σ_r in the cases without the LEM. Therefore, the *narrowing mixing scenario* can affect the DSDs in the entire cloud, even with its rare occurrence.

6. Summary and Conclusion

This study investigated different effects on the cloud DSD resulting from different mixing scenarios in a cumulus congestus cloud, applying the IHMD metric to classify mixing scenarios ranging between homogeneous and inhomogeneous. This study used a LES model coupled with a LCM to simulate cloud microphysics, and a SGS LEM to represent unresolved turbulent mixing. The LEM allows the effects of mixing between homogeneous and inhomogeneous to be realistically represented in the three-dimensional model based on the local relative humidity, turbulent dissipation rate, and DSD shape.

We investigated three distinctive ways how the DSD width changes due to mixing.

1. In the homogeneous mixing scenario, the DSD is broadened toward smaller droplets after mixing. This scenario occurs when the entrained air is relatively dry and the microphysical response time, especially the evaporation timescale, is relatively long as expected from theory (e.g., Baker & Latham, 1979).
2. In the inhomogeneous mixing scenario, only droplets in subsaturated regions of the cloud evaporate completely, while others in saturated regions remain unchanged, causing the DSD width and droplet mean volume radius to remain relatively constant compared to the homogeneous mixing case. The inhomogeneous

mixing is favored when the evaporation timescale is relatively short and entrained air is relatively humid, in agreement with theory (e.g., Baker & Latham, 1979).

3. Most interestingly, we found a *narrowing mixing scenario* that reduces the DSD width, where only small droplets completely evaporate while large droplets remain unchanged, resulting in an increase in droplet mean volume radius that cannot be subjected to the two traditional mixing scenarios (e.g., Krueger et al., 2008; Luo et al., 2022; Pinsky et al., 2016; Tölle & Krueger, 2014).

We showed that droplet-size dependant evaporation plays an important role in the *narrowing mixing scenario* (Luo et al., 2020, 2021; Pinsky et al., 2016; Tölle & Krueger, 2014). Small droplets may evaporate completely before large droplets change substantially. Thus, when the relative dispersion of the DSD is large and contains numerous small droplets, complete evaporation of small droplets, which evaporate faster, becomes sufficient to restore saturation without substantially affecting the size of the larger droplets. High relative humidities of cloudy and entrained air, and an updraft, producing additional supersaturation, make this scenario more likely (Luo et al., 2022).

While this study investigated a cloud where secondary activation of entrained aerosol particles is insignificant, we also confirmed that secondary activation during ascent could be related to the DSD shape changes during mixing. We showed secondary activation during mixing leads to DSD broadening and amplifies the effect of homogeneous mixing (Krueger et al., 2008; Luo et al., 2022). However, we found that in the *narrowing mixing scenario*, significant complete evaporation of small droplets, that is, deactivation, leads to a negligible *net* droplet activation rate during ascent. Therefore, to understand the role of secondary activation during mixing better, we suggest considering the *net* activation rate during mixing rather than the activation rate alone. Furthermore, the parcel models used in the aforementioned studies tend to artificially lift detrained air, potentially overestimating the secondary activation of previously detrained aerosols. Our simulations represent this process more naturally by dispersing these particles outside the cloud, preventing their immediate re-activation.

This study suggests that SGS mixing parameterizations, such as the IHMD, should also take into account other parameters, such as DSD shape, ascending motion, and relative humidity. Promising approaches to consider the DSD width (Luo et al., 2021) and the relative humidity (Xu et al., 2022) can be found in the literature. Our work also suggests the need for further studies on the spatial and temporal distribution of the IHMD during the entire cloud lifecycle and across different cloud types, which affect microphysical parameters related to the mixing scenarios (Lehmann et al., 2009; Schmeissner et al., 2015). Combining all these efforts will help the development of SGS mixing parameterizations for a better representation of DSD changes in the future.

Finally, we found that entrainment and mixing favor a relative dispersion of the DSD 0.2 to 0.4, which is typical for non-precipitating cumulus clouds (Yum & Hudson, 2005). Too narrow distributions are prevented by homogeneous mixing leading to broadening, while the *narrowing mixing scenario* might explain why extremely wide DSDs are rarely found in clouds in the absence of precipitation. Unfortunately, the distinct ways entrainment and mixing change the DSD can be overlooked in simulations without proper consideration of the SGS turbulent mixing or without the proper consideration of the large-scale cloud dynamics. In fact, our simulations without the LEM tend to mix more homogeneously with less *narrowing mixing*, and clouds have broader DSDs than with the LEM. Along with numerical diffusion that is suggested to erroneously widen DSDs modeled with bin cloud microphysics (Grabowski et al., 2019; Morrison et al., 2018), the assumption of pure homogeneous mixing assumption can also be a reason why DSD widths are often overestimated in conventional cloud microphysical models. Therefore, considering all relevant scales of entrainment and mixing down to the millimeter scale will be essential to predict a realistic DSD evolution.

Data Availability Statement

The System for Atmospheric Modeling (SAM) code is available under the link http://rossby.msrc.sunysb.edu/SAM.html, with permission from its developer Dr. M. Khairoutdinov (Khairoutdinov & Randall, 2003). The simulation results are available under the link https://doi.org/10.5281/zenodo.7120916 (Lim & Hoffmann, 2022). Figures are made with Matplotlib version 3.3.4, available under the link https://matplotlib.org/.

References

Andrejczuk, M., Grabowski, W. W., Malinowski, S. P., & Smolarkiewicz, P. K. (2006). Numerical simulation of cloud–clear air interfacial mixing: Effects on cloud microphysics. *Journal of the Atmospheric Sciences*, *63*(12), 3204–3225. https://doi.org/10.1175/JAS3813.1

Baker, M., Corbin, R., & Latham, J. (1980). The influence of entrainment on the evolution of cloud droplet spectra: I. A model of inhomogeneous mixing. *Quarterly Journal of the Royal Meteorological Society*, *106*(449), 581–598. https://doi.org/10.1002/qj.49710644914

Baker, M., & Latham, J. (1979). The evolution of droplet spectra and the rate of production of embryonic raindrops in small cumulus clouds. *Journal of the Atmospheric Sciences*, *36*(8), 1612–1615. https://doi.org/10.1175/1520-0469(1979)036%3C1612:TEODSA%3E2.0.CO;2

Blyth, A. M. (1993). Entrainment in cumulus clouds. *Journal of Applied Meteorology and Climatology*, *32*(4), 626–641. https://doi.org/10.1175/1520-0450(1993)032⟨0626:EICC⟩2.0.CO;2

Boucher, O., Randall, D., Artaxo, P., Bretherton, C., Feingold, G., Forster, P., et al. (2013). Clouds and aerosols. In *Climate change 2013: The physical science basis. Contribution of working group I to the fifth assessment report of the intergovernmental panel on climate change* (pp. 571–657). Cambridge University Press.

Burnet, F., & Brenguier, J.-L. (2007). Observational study of the entrainment-mixing process in warm convective clouds. *Journal of the Atmospheric Sciences*, *64*(6), 1995–2011. https://doi.org/10.1175/JAS3928.1

Chandrakar, K. K., Grabowski, W. W., Morrison, H., & Bryan, G. H. (2021). Impact of entrainment mixing and turbulent fluctuations on droplet size distributions in a cumulus cloud: An investigation using Lagrangian microphysics with a subgrid-scale model. *Journal of the Atmospheric Sciences*, *78*(9), 2983–3005. https://doi.org/10.1175/JAS-D-20-0281.1

Chosson, F., Brenguier, J.-L., & Schüller, L. (2007). Entrainment-mixing and radiative transfer simulation in boundary layer clouds. *Journal of the Atmospheric Sciences*, *64*(7), 2670–2682. https://doi.org/10.1175/JAS3975.1

Desai, N., Liu, Y., Glienke, S., Shaw, R. A., Lu, C., Wang, J., & Gao, S. (2021). Vertical variation of turbulent entrainment mixing processes in marine stratocumulus clouds using high-resolution digital holography. *Journal of Geophysical Research: Atmospheres*, *126*(7), e2020JD033527. https://doi.org/10.1029/2020JD033527

Devenish, B., Bartello, P., Brenguier, J., Collins, L., Grabowski, W. W., Ijzermans, R., et al. (2012). Droplet growth in warm turbulent clouds. *Quarterly Journal of the Royal Meteorological Society*, *138*(667), 1401–1429. https://doi.org/10.1002/qj.1897

Eytan, E., Koren, I., Altaratz, O., Pinsky, M., & Khain, A. (2021). What is adiabatic fraction in cumulus clouds: High-resolution simulations with passive tracer. *Atmospheric Chemistry and Physics Discussions*, 2021, 1–23. https://doi.org/10.5194/acp-2021-334

Gao, Z., Liu, Y., Li, X., & Lu, C. (2018). Investigation of turbulent entrainment-mixing processes with a new particle-resolved direct numerical simulation model. *Journal of Geophysical Research: Atmospheres*, *123*(4), 2194–2214. https://doi.org/10.1002/2017JD027507

Gao, S., Lu, C., Liu, Y., Mei, F., Wang, J., Zhu, L., & Yan, S. (2020). Contrasting scale dependence of entrainment-mixing mechanisms in stratocumulus clouds. *Geophysical Research Letters*, *47*(9), e2020GL086970. https://doi.org/10.1029/2020GL086970

Gerber, H. E., Frick, G. M., Jensen, J. B., & Hudson, J. G. (2008). Entrainment, mixing, and microphysics in trade-wind cumulus. *Journal of the Meteorological Society of Japan Series II*, *86*, 87–106. https://doi.org/10.2151/jmsj.86A.87

Grabowski, W. W. (2006). Indirect impact of atmospheric aerosols in idealized simulations of convective–radiative quasi equilibrium. *Journal of Climate*, *19*(18), 4664–4682. https://doi.org/10.1175/JCLI3857.1

Grabowski, W. W., Morrison, H., Shima, S.-I., Abade, G. C., Dziekan, P., & Pawlowska, H. (2019). Modeling of cloud microphysics: Can we do better? *Bulletin of the American Meteorological Society*, *100*(4), 655–672. https://doi.org/10.1175/BAMS-D-18-0005.1

Grabowski, W. W., & Wang, L.-P. (2013). Growth of cloud droplets in a turbulent environment. *Annual Review of Fluid Mechanics*, *45*(1), 293–324. https://doi.org/10.1146/annurev-fluid-011212-140750

Heus, T., & Jonker, H. J. (2008). Subsiding shells around shallow cumulus clouds. *Journal of the Atmospheric Sciences*, *65*(3), 1003–1018. https://doi.org/10.1175/2007JAS2322.1

Hoffmann, F. (2020). Effects of entrainment and mixing on the wegener–bergeron–findeisen process. *Journal of the Atmospheric Sciences*, *77*(6), 2279–2296. https://doi.org/10.1175/JAS-D-19-0289.1

Hoffmann, F., & Feingold, G. (2019). Entrainment and mixing in stratocumulus: Effects of a new explicit subgrid-scale scheme for large-eddy simulations with particle-based microphysics. *Journal of the Atmospheric Sciences*, *76*(7), 1955–1973. https://doi.org/10.1175/JAS-D-18-0318.1

Hoffmann, F., Raasch, S., & Noh, Y. (2015). Entrainment of aerosols and their activation in a shallow cumulus cloud studied with a coupled LCM–LES approach. *Atmospheric Research*, *156*, 43–57. https://doi.org/10.1016/j.atmosres.2014.12.008

Hoffmann, F., Yamaguchi, T., & Feingold, G. (2019). Inhomogeneous mixing in Lagrangian cloud models: Effects on the production of precipitation embryos. *Journal of the Atmospheric Sciences*, *76*(1), 113–133. https://doi.org/10.1175/JAS-D-18-0087.1

Jarecka, D., Grabowski, W. W., Morrison, H., & Pawlowska, H. (2013). Homogeneity of the subgrid-scale turbulent mixing in large-eddy simulation of shallow convection. *Journal of the Atmospheric Sciences*, *70*(9), 2751–2767. https://doi.org/10.1175/JAS-D-13-042.1

Kerstein, A. R. (1988). A linear-eddy model of turbulent scalar transport and mixing. *Combustion Science and Technology*, *60*(4–6), 391–421. https://doi.org/10.1080/00102208808923995

Khairoutdinov, M. F., & Randall, D. A. (2003). Cloud resolving modeling of the arm summer 1997 iop: Model formulation, results, uncertainties, and sensitivities. *Journal of the Atmospheric Sciences*, *60*(4), 607–625. https://doi.org/10.1175/1520-0469(2003)060%3C0607:CRMOTA%3E2.0.CO;2

Kogan, Y. L. (1991). The simulation of a convective cloud in a 3-d model with explicit microphysics. Part I: Model description and sensitivity experiments. *Journal of the Atmospheric Sciences*, *48*(9), 1160–1189. https://doi.org/10.1175/1520-0469(1991)048%3C1160:TSOACC%3E2.0.CO;2

Korolev, A., Khain, A., Pinsky, M., & French, J. (2016). Theoretical study of mixing in liquid clouds–part 1: Classical concepts. *Atmospheric Chemistry and Physics*, *16*(14), 9235–9254. https://doi.org/10.5194/acp-16-9235-2016

Korolev, A. V., & Mazin, I. P. (2003). Supersaturation of water vapor in clouds. *Journal of the Atmospheric Sciences*, *60*(24), 2957–2974. https://doi.org/10.1175/1520-0469(2003)060%3C2957:SOWVIC%3E2.0.CO;2

Krueger, S. K. (1993). Linear eddy modeling of entrainment and mixing in stratus clouds. *Journal of the Atmospheric Sciences*, *50*(18), 3078–3090. https://doi.org/10.1175/1520-0469(1993)050%3C3078:LEMOEA%3E2.0.CO;2

Krueger, S. K., Schlueter, H., & Lehr, P. (2008). Fine-scale modeling of entrainment and mixing of cloudy and clear air. *Paper presented at 15th International Conference on Clouds and Precipitation, Cancun, Mexico.*

Krueger, S. K., Su, C.-W., & McMurtry, P. A. (1997). Modeling entrainment and finescale mixing in cumulus clouds. *Journal of the Atmospheric Sciences*, *54*(23), 2697–2712. https://doi.org/10.1175/1520-0469(1997)054⟨2697:MEAFMI⟩2.0.CO;2

Kumar, B., Bera, S., Prabha, T. V., & Grabowski, W. W. (2017). Cloud-edge mixing: Direct numerical simulation and observations in Indian monsoon clouds. *Journal of Advances in Modeling Earth Systems*, *9*(1), 332–353. https://doi.org/10.1002/2016MS000731

Kumar, B., Schumacher, J., & Shaw, R. A. (2013). Cloud microphysical effects of turbulent mixing and entrainment. *Theoretical and Computational Fluid Dynamics*, *27*(3), 361–376. https://doi.org/10.1007/s00162-012-0272-z

Lasher-Trapp, S. G., Cooper, W. A., & Blyth, A. M. (2005). Broadening of droplet size distributions from entrainment and mixing in a cumulus cloud. *Quarterly Journal of the Royal Meteorological Society*, *131*(605), 195–220. https://doi.org/10.1256/qj.03.199

Lehmann, K., Siebert, H., & Shaw, R. A. (2009). Homogeneous and inhomogeneous mixing in cumulus clouds: Dependence on local turbulence structure. *Journal of the Atmospheric Sciences*, *66*(12), 3641–3659. https://doi.org/10.1175/2009JAS3012.1

Lim, J.-S., & Hoffmann, F. (2022). SAM simulation output [Dataset]. Zenodo. https://doi.org/10.5281/zenodo.7629939

Lu, C., Liu, Y., Niu, S., & Endo, S. (2014). Scale dependence of entrainment-mixing mechanisms in cumulus clouds. *Journal of Geophysical Research: Atmospheres*, *119*(24), 13–877. https://doi.org/10.1002/2014JD022265

Lu, C., Liu, Y., Niu, S., Krueger, S., & Wagner, T. (2013). Exploring parameterization for turbulent entrainment-mixing processes in clouds. *Journal of Geophysical Research: Atmospheres*, *118*(1), 185–194. https://doi.org/10.1029/2012JD018464

Lu, C., Liu, Y., Yum, S. S., Chen, J., Zhu, L., Gao, S., et al. (2020). Reconciling contrasting relationships between relative dispersion and volume-mean radius of cloud droplet size distributions. *Journal of Geophysical Research: Atmospheres*, *125*(9), e2019JD031868. https://doi.org/10.1029/2019JD031868

Lu, C., Liu, Y., Zhu, B., Yum, S. S., Krueger, S. K., Qiu, Y., et al. (2018). On which microphysical time scales to use in studies of entrainment-mixing mechanisms in clouds. *Journal of Geophysical Research: Atmospheres*, *123*(7), 3740–3756. https://doi.org/10.1002/2017JD027985

Luo, S., Lu, C., Liu, Y., Bian, J., Gao, W., Li, J., et al. (2020). Parameterizations of entrainment-mixing mechanisms and their effects on cloud droplet spectral width based on numerical simulations. *Journal of Geophysical Research: Atmospheres*, *125*(22), e2020JD032972. https://doi.org/10.1029/2020JD032972

Luo, S., Lu, C., Liu, Y., Gao, W., Zhu, L., Xu, X., et al. (2021). Consideration of initial cloud droplet size distribution shapes in quantifying different entrainment-mixing mechanisms. *Journal of Geophysical Research: Atmospheres*, *126*(13), e2020JD034455. https://doi.org/10.1029/2020JD034455

Luo, S., Lu, C., Liu, Y., Li, Y., Gao, W., Qiu, Y., et al. (2022). Relationships between cloud droplet spectral relative dispersion and entrainment rate and their impacting factors. *Advances in Atmospheric Sciences*, *39*(12), 1–20. https://doi.org/10.1007/s00376-022-1419-5

Mordy, W. (1959). Computations of the growth by condensation of a population of cloud droplets. *Tellus*, *11*(1), 16–44. https://doi.org/10.1111/j.2153-3490.1959.tb00003.x

Morrison, H., & Grabowski, W. W. (2008). Modeling supersaturation and subgrid-scale mixing with two-moment bulk warm microphysics. *Journal of the Atmospheric Sciences*, *65*(3), 792–812. https://doi.org/10.1175/2007JAS2374.1

Morrison, H., Witte, M., Bryan, G. H., Harrington, J. Y., & Lebo, Z. J. (2018). Broadening of modeled cloud droplet spectra using bin microphysics in an Eulerian spatial domain. *Journal of the Atmospheric Sciences*, *75*(11), 4005–4030. https://doi.org/10.1175/JAS-D-18-0055.1

Oh, D., & Noh, Y. (2022). Roles of drop size distribution and turbulence in autoconversion based on Lagrangian cloud model simulations. *Journal of Geophysical Research: Atmospheres*, *127*(16), e2022JD036495. https://doi.org/10.1029/2022JD036495

Pinsky, M., Khain, A., Korolev, A., & Magaritz-Ronen, L. (2016). Theoretical investigation of mixing in warm clouds–part 2: Homogeneous mixing. *Atmospheric Chemistry and Physics*, *16*(14), 9255–9272. https://doi.org/10.5194/acp-16-9255-2016

Schmeissner, T., Shaw, R., Ditas, J., Stratmann, F., Wendisch, M., & Siebert, H. (2015). Turbulent mixing in shallow trade wind cumuli: Dependence on cloud life cycle. *Journal of the Atmospheric Sciences*, *72*(4), 1447–1465. https://doi.org/10.1175/JAS-D-14-0230.1

Shima, S.-i., Kusano, K., Kawano, A., Sugiyama, T., & Kawahara, S. (2009). The super-droplet method for the numerical simulation of clouds and precipitation: A particle-based and probabilistic microphysics model coupled with a non-hydrostatic model. *Quarterly Journal of the Royal Meteorological Society*, *135*(642), 1307–1320. https://doi.org/10.1002/qj.441

Shima, S.-i., Sato, Y., Hashimoto, A., & Misumi, R. (2020). Predicting the morphology of ice particles in deep convection using the super-droplet method: Development and evaluation of scale-SDM 0.2. 5-2.2. 0,-2.2. 1, and-2.2. 2. *Geoscientific Model Development*, *13*(9), 4107–4157. https://doi.org/10.5194/gmd-13-4107-2020

Slawinska, J., Grabowski, W. W., Pawlowska, H., & Wyszogrodzki, A. A. (2008). Optical properties of shallow convective clouds diagnosed from a bulk-microphysics large-eddy simulation. *Journal of Climate*, *21*(7), 1639–1647. https://doi.org/10.1175/2007JCLI1820.1

Squires, P. (1952). The growth of cloud drops by condensation. i. general characteristics. *Australian Journal of Chemistry*, *5*(1), 59–86. https://doi.org/10.1071/CH9520059

Su, C.-W., Krueger, S. K., McMurtry, P. A., & Austin, P. H. (1998). Linear eddy modeling of droplet spectral evolution during entrainment and mixing in cumulus clouds. *Atmospheric Research*, *47*, 41–58. https://doi.org/10.1016/S0169-8095(98)00039-8

Tölle, M. H., & Krueger, S. K. (2014). Effects of entrainment and mixing on droplet size distributions in warm cumulus clouds. *Journal of Advances in Modeling Earth Systems*, *6*(2), 281–299. https://doi.org/10.1002/2012MS000209

Xu, X., Lu, C., Liu, Y., Luo, S., Zhou, X., Endo, S., et al. (2022). Influences of an entrainment–mixing parameterization on numerical simulations of cumulus and stratocumulus clouds. *Atmospheric Chemistry and Physics*, *22*(8), 5459–5475. https://doi.org/10.5194/acp-22-5459-2022

Yau, M. K., & Rogers, R. R. (1996). *A short course in cloud physics*. Elsevier.

Yum, S. S., & Hudson, J. G. (2005). Adiabatic predictions and observations of cloud droplet spectral broadness. *Atmospheric Research*, *73*(3–4), 203–223. https://doi.org/10.1016/j.atmosres.2004.10.006

Yum, S. S., Wang, J., Liu, Y., Senum, G., Springston, S., McGraw, R., & Yeom, J. M. (2015). Cloud microphysical relationships and their implication on entrainment and mixing mechanism for the stratocumulus clouds measured during the vocals project. *Journal of Geophysical Research: Atmospheres*, *120*(10), 5047–5069. https://doi.org/10.1002/2014JD022802